RSC Advances

PAPER

View Article Online
View Journal | View Issue

Cite this: *RSC Adv.*, 2018, **8**, 16521

Li^+ conductivity of tungsten bronze $Li_xSr_{1-0.5x}Ta_2O_6$ studied by neutron diffraction analysis†

Hyeon-Dong Han,[a] Maxim Avdeev [bc] and Young-Il Kim *[a]

Received 30th March 2018
Accepted 28th April 2018

DOI: 10.1039/c8ra02779j

rsc.li/rsc-advances

The crystal structures of tetragonal tungsten bronze, $Li_xSr_{1-0.5x}Ta_2O_6$ (x = 0.08, 0.17, 0.25) were investigated by neutron diffraction analysis, focusing on the geometry of the oxide framework as well as the Li distribution. The Rietveld refinement and Fourier mapping of nuclear density indicated that Li atoms are distributed in the pentagonal and rectangular channels of the tungsten bronze lattice, which provide 15-fold and 12-fold coordinated cavities, respectively. Those cavities are interconnected to form a three-dimensional network, which can serve as the Li^+ conduction pathway in $Li_xSr_{1-0.5x}Ta_2O_6$. It is proposed that the rhombic faces of the 12-coordinated polyhedra (distorted cuboctahedra) act as the bottleneck for long-range Li^+ migration.

1. Introduction

Tungsten bronze type structures possess unique 1-dimensional channels running along the crystal c-axis, which is promising for the insertion/exchange of small cations such as Li^+.[1–8] In the tetragonal tungsten bronzes (TTBs), three types of c-directional channels are found: the ab unit area ($\approx 12.4 \times 12.4$ Å^2) contains four pentagonal channels, two quadrangular channels, and four triangular channels, with 15, 12, and 9-coordinated cavities, respectively (Fig. 1).[9,10] The ionic conductivity of tungsten bronzes has been reported from several different phases such as $A_{0.6}(M, Nb)O_3$ (A = Sr, Ba; M = Mg, Ti), $Pb_{5-x}K_{6(1-x)}Li_{4(1-x)}Ta_{10}O_{30}$, $Ba_{0.22}TaO_{0.72}$, and $Na_{1-x}H_xNbWO_6 \cdot yH_2O$.[11–18] In the above, the position of mobile Li^+ or H^+ has been estimated diversely depending on the composition, triangular channel in $Pb_{5-x}K_{6(1-x)}Li_{4(1-x)}Ta_{10}O_{30}$ and $Pb_{5(1-x)}Li_{10x}Ta_{10}O_{30}$,[12,15] and pentagonal channel in $H_{0.8}Na_{0.4}Nb_{1.2}W_{0.8}O_6$.[16]

Recently, lithiation of the TTB oxide β-$SrTa_2O_6$ was accomplished by a solid state ion exchange of $Sr^{2+} \rightarrow 2Li^+$.[19] The ionic conductivity of $Li_xSr_{1-0.5x}Ta_2O_6$, as a function of Li content, $0 < x \leq 0.31$, was highest for $x \approx 0.17$ ($\sigma = 10^{-5}\ \Omega^{-1}\ cm^{-1}$ at 540 K). The scanning and transmission electron microscopic studies strongly suggested that the Li^+/Sr^{2+} diffusion in $Li_xSr_{1-0.5x}Ta_2O_6$ occurred along the channel direction (c-axis). As the Sr^{2+} ions in β-$SrTa_2O_6$ occupy the pentagonal and tetragonal channels, it can be conjectured that Li^+ ions enter either or both of the above sites, although the distribution of Li^+ has not been definitely judged for $Li_xSr_{1-0.5x}Ta_2O_6$.

For better understanding the cation exchange process and the ionic transport in $Li_xSr_{1-0.5x}Ta_2O_6$, neutron powder diffraction was carried out for three different compositions, x = 0.08, 0.17, and 0.25. The Rietveld refinement and Fourier mapping of the nuclear scattering density were performed, focusing on the Li^+ locations in $Li_xSr_{1-0.5x}Ta_2O_6$. It is shown that the 12-coordinate cavities inside the quadrangular channel of $Li_xSr_{1-0.5x}Ta_2O_6$ are capped with six rhombic faces, the size of which varies along the progress of the lithiation, possibly impacting on the activation barrier of the ion hopping.

2. Experimental

The tungsten bronze oxide β-$SrTa_2O_6$ was prepared *via* a solid state reaction using $SrCO_3$ (Alfa Aesar, 99.95%) and Ta_2O_5 (Alfa Aesar, 99.95%), with a final heating temperature of 1673 K.[20] For preparing $Li_xSr_{1-0.5x}Ta_2O_6$ (x = 0.08, 0.17, and 0.25), a mixture of polycrystalline Li_2CO_3 (Aldrich, 99.99%) and β-$SrTa_2O_6$ was heated to 873 K in air for 12 h. After heating, the sample was rinsed with distilled water, and dried in air at 328 K for 12 h.[19] The Li concentration of the product sample was controlled by varying the Li : Sr ratio in the starting reactant mixture. The chemical analysis, lattice constants, and ionic conductivity of $Li_xSr_{1-0.5x}Ta_2O_6$ were reported in a previous work.[19]

Powder neutron diffraction (ND) was measured for $Li_xSr_{1-0.5x}Ta_2O_6$ (x = 0.08, 0.17, and 0.25) in the powder diffractometer, Echidna, at the Australian Nuclear Science Technology Organisation's OPAL facility. The ND data was recorded using $\approx$2 g of powder sample loaded in a vanadium can, with λ = 2.4395 Å over the 2θ range, 10–164°, at a step size 0.05°. The

[a]Department of Chemistry, Graduate School, Yeungnam University, Gyeongsan 38541, Republic of Korea. E-mail: yikim@ynu.ac.kr; Fax: +82 53 810 4613

[b]Australian Centre for Neutron Scattering, Australian Nuclear Science and Technology Organisation, Locked Bag 2001, Kirrawee DC, NSW 2232, Australia

[c]School of Chemistry, The University of Sydney, Sydney, NSW 2006, Australia

† Electronic supplementary information (ESI) available. See DOI: 10.1039/c8ra02779j

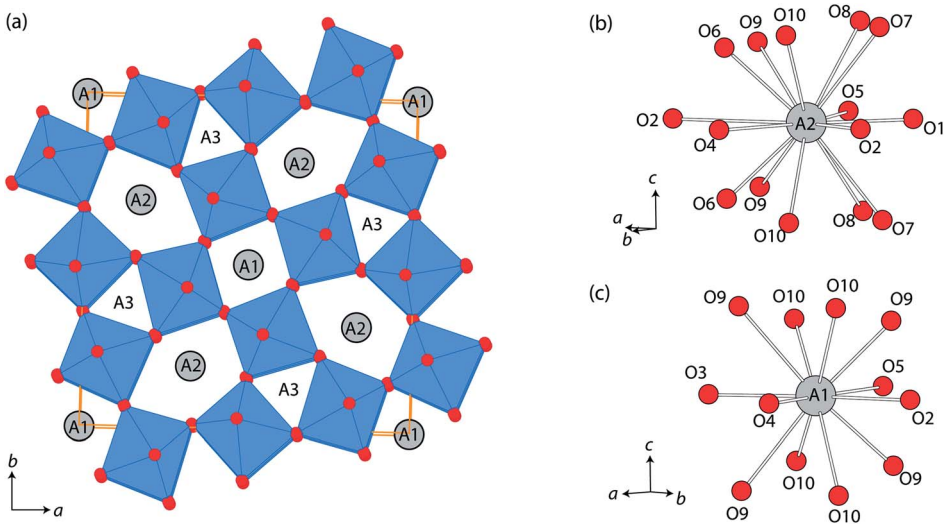

Fig. 1 (a) Crystal structure of tetragonal tungsten bronze projected along *c*-axis, and the coordination environments of (b) A2 and (c) A1 sites, using a particular example of β-$SrTa_2O_6$.

Rietveld refinement and Fourier map calculation were carried out using the GSAS-EXPGUI software suite.[21,22]

3. Results and discussion

Fig. 2 shows the ionic conductivity of $Li_xSr_{1-0.5x}Ta_2O_6$ as a function of x, measured in the temperature range 298–540 K. The above data were acquired in the dry N_2 atmosphere and represent the Li^+ conductivity (σ_{Li}) of $Li_xSr_{1-0.5x}Ta_2O_6$. Notably, the maximal σ_{Li} occurred around $x = 0.17$, which was interpreted as the compromise between structural and compositional factors. The increase of Li content in $Li_xSr_{1-0.5x}Ta_2O_6$ accompanied the contractions of the *ab*-dimension and hence the cross-sectional area of the potential Li pathways. That is, the increase of carrier concentration was likely counteracted by the decrease of carrier mobility.

Although the previous study by synchrotron X-ray diffraction (XRD) determined the crystal symmetry and lattice constants of $Li_xSr_{1-0.5x}Ta_2O_6$,[19] the detailed information on Li occupancy could not be obtained mainly due to its insignificant scattering power. As a complementary approach, neutron powder diffraction was employed here. The neutron scattering length (b) of Li is of comparable magnitude to those of other elements contained in $Li_xSr_{1-0.5x}Ta_2O_6$,[23,24] which makes the ND data useful for the structural study.

It was supposed that $Li_xSr_{1-0.5x}Ta_2O_6$ had quite similar structures to that of β-$SrTa_2O_6$, and therefore the neutron Rietveld refinements of $Li_xSr_{1-0.5x}Ta_2O_6$ used a structure model based on β-$SrTa_2O_6$ (Fig. 1).[20] In practice, the Rietveld refinement of $Li_xSr_{1-0.5x}Ta_2O_6$ was conducted in a semi-constrained

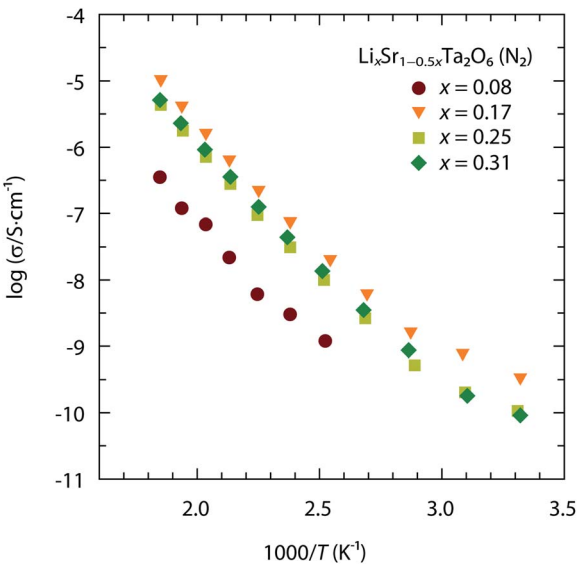

Fig. 2 Temperature-dependent ionic conductivity of $Li_xSr_{1-0.5x}Ta_2O_6$ ($x = 0.08$, 0.17, 0.25, and 0.31) measured in N_2.

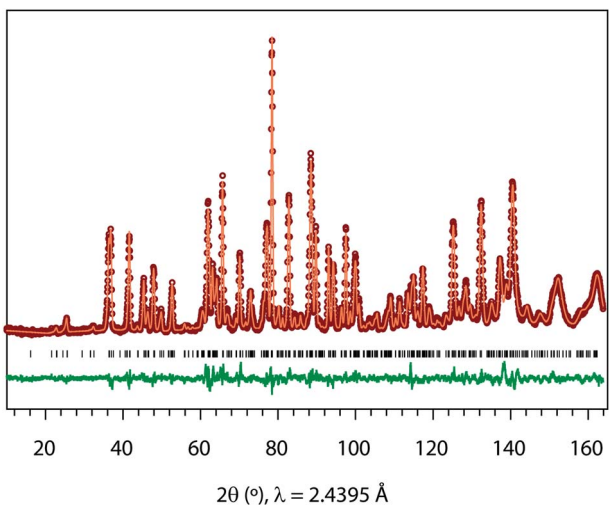

Fig. 3 Neutron Rietveld refinement of $Li_{0.08}Sr_{0.96}Ta_2O_6$ ($R_{wp} = 5.94\%$, $R_p = 4.72\%$, $\chi^2 = 1.25$).

Table 1 Atomic parameters of $Li_{0.08}Sr_{0.96}Ta_2O_6$ obtained from neutron Rietveld refinement[a]

Atom		x	y	z	U_{iso} (Å^2)	occ
Sr1[b]	4c	0.997(1)	0.001(2)	0.25	0.001[c]	0.581(7)[d]
Sr2[b]	4c	0.3487(8)	0.1859(9)	0.25	0.015[c]	0.885(4)[d]
Sr3[b]	4c	0.3374(8)	0.1869(1)	0.75	0.015[c]	0.885(4)[d]
Ta1	4b	0	0.5	0.5	0.0015[c]	1
Ta2	8d	0.0735(4)	0.2080(4)	0.4985(8)	0.0015[c]	1
Ta3	8d	0.2860(4)	0.4242(4)	0.5049(9)	0.0015[c]	1
O1	4c	0.9824(8)	0.4721(8)	0.25	0.0174(9)	1
O2	4c	0.0525(8)	0.2195(10)	0.25	0.0174(9)	1
O3	4c	0.1121(9)	0.1914(8)	0.75	0.0174(9)	1
O4	4c	0.3199(7)	0.4201(9)	0.25	0.0174(9)	1
O5	4c	0.2726(8)	0.4143(10)	0.75	0.0174(9)	1
O6	8d	0.2234(5)	0.2743(5)	0.4767(8)	0.002(1)	1
O7	8d	−0.0006(6)	0.3463(6)	0.5385(9)	0.019(1)	1
O8	8d	0.3414(6)	0.0066(6)	0.5361(9)	0.019(1)	1
O9	8d	0.1344(6)	0.0621(6)	0.468(1)	0.027(1)	1
O10	8d	0.4353(7)	0.3537(6)	0.530(1)	0.027(1)	1

[a] Space group *Pnam* ($Z = 10$), $a = 12.3604(3)$ Å, $b = 12.4137(4)$ Å, $c = 7.7207(2)$ Å. [b] Sr1 site corresponds to quadrangular cavity (A1 in Fig. 1); Sr2 and Sr3 sites correspond to pentagonal cavity (A2 in Fig. 1). [c] Fixed. [d] Occupancy factors (occ) for Sr1, Sr2, and Sr3 sites represent the combined contribution from Sr and Li, and are expressed in terms of the neutron scattering length of Sr.

manner. While the lattice constants and all the atomic positions were fully refined, the site occupancies for Sr/Li were subjected to two constraints. First, the amounts of Li and Sr were fixed according to the result of chemical analysis for three samples, which were $Li_{0.08}Sr_{0.96}Ta_2O_6$, $Li_{0.17}Sr_{0.92}Ta_2O_6$, and $Li_{0.25}Sr_{0.88}Ta_2O_6$, respectively. Second, Li was distributed only to pentagonal and quadrangular channels, *i.e.*, the A2 and A1 sites shown in Fig. 1.

Fig. 3 shows, as an example, the refinement profile for $Li_{0.08}Sr_{0.96}Ta_2O_6$, and Table 1 lists the corresponding atomic parameters. The plots for $x = 0.17$ and 0.25, and the associated structural parameters are included in ESI.† Fig. 4 summarizes the structural evolutions upon the Li introduction to β-$SrTa_2O_6$. The unit cell volume of $Li_xSr_{1-0.5x}Ta_2O_6$ gradually decreased with increasing x (Fig. 4c), which confirmed the observation from the previous XRD study.[19] Such a result is attributed mainly to the smaller size of Li^+ as compared with Sr^{2+}.[25]

In the neutron Rietveld refinement, it was of main interest to examine the occupancies (occ) of A1 and A2 sites. The model structure of β-$SrTa_2O_6$, which is an orthorhombic TTB, is rather complex and includes a large number of structural variables.[20] Partly because of such a complexity, the site occupancies of $Li_xSr_{1-0.5x}Ta_2O_6$ were refined under the aforementioned constraints.

The coherent neutron scattering lengths of Li and Sr are −1.90 fm and 7.02 fm, respectively. Therefore, either the Li population or the Sr vacation will only decrease the nuclear density for a given site (A1 or A2). Fig. 5 shows the effective neutron scattering lengths (b_{eff}) for the A1 and A2 sites, where $b_{eff} = 7.02 \times occ(Sr) - 1.90 \times occ(Li)$. With the increase of x in $Li_xSr_{1-0.5x}Ta_2O_6$, the b_{eff}(A1) decreased more rapidly than b_{eff}(A2). It implies that the $Sr^{2+} \rightarrow 2Li^+$ exchange occurred more frequently in the quadrangular channel than in the pentagonal channel, and also that Li^+ preferred the A1 site. Such a result is reasonable when considering the small size of Li^+. In fact, there were several cases where Li^+ occupied even the 9-coordinated A3 site within the triangular channel.[9,12,15]

The orthorhombic distortion of β-$SrTa_2O_6$ was lessened by the Li/Sr exchange, and this can also be attributed to the size effect. The A1 site of β-$SrTa_2O_6$ is somewhat smaller than Sr^{2+}. As a quick indicator, the bond valence sum (BVS) for Sr, when located at the A1 site of β-$SrTa_2O_6$, is calculated to be 2.53 valence units[20] and the corresponding value becomes even larger in $Li_xSr_{1-0.5x}Ta_2O_6$. On the other hand, Li is grossly

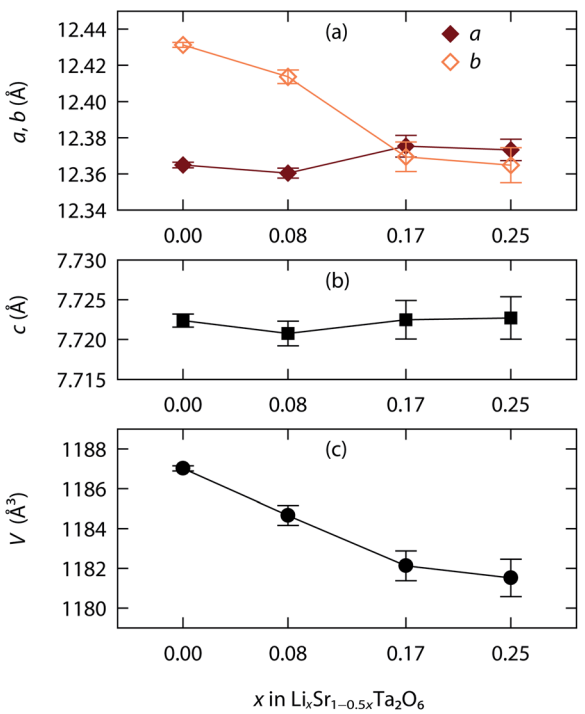

Fig. 4 Lattice evolution upon the Li^+/Sr^{2+} ion exchange in β-$SrTa_2O_6$: (a) a, b parameters, (b) c parameter, and (c) unit cell volume.

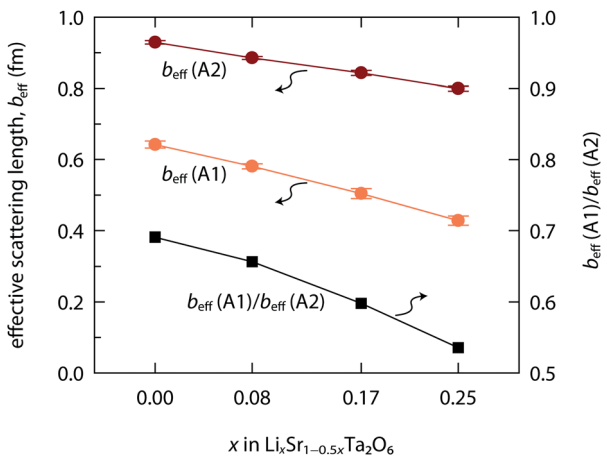

Fig. 5 Effective neutron scattering lengths (b_{eff}) evaluated for Sr/Li sites, A1 and A2, in $Li_xSr_{1-0.5x}Ta_2O_6$ ($x = 0$, 0.08, 0.17, and 0.25).

Table 2 Nuclear scattering density (fm Å^{-3}) at the peaks identified from the observed (ρ_{obs}) and difference (ρ_{diff}) Fourier profiles

	β-$SrTa_2O_6$	$Li_{0.08}Sr_{0.96}Ta_2O_6$	$Li_{0.17}Sr_{0.92}Ta_2O_6$	$Li_{0.25}Sr_{0.88}Ta_2O_6$
$\rho_{obs,\ max}$	1.690	1.702	1.684	1.679
$\rho_{obs,\ min}$	−0.505	−0.448	−0.405	−0.414
$\rho_{diff,\ max}$	0.028	0.033	0.078	0.079
$\rho_{diff,\ min}$	−0.025	−0.028	−0.067	−0.069

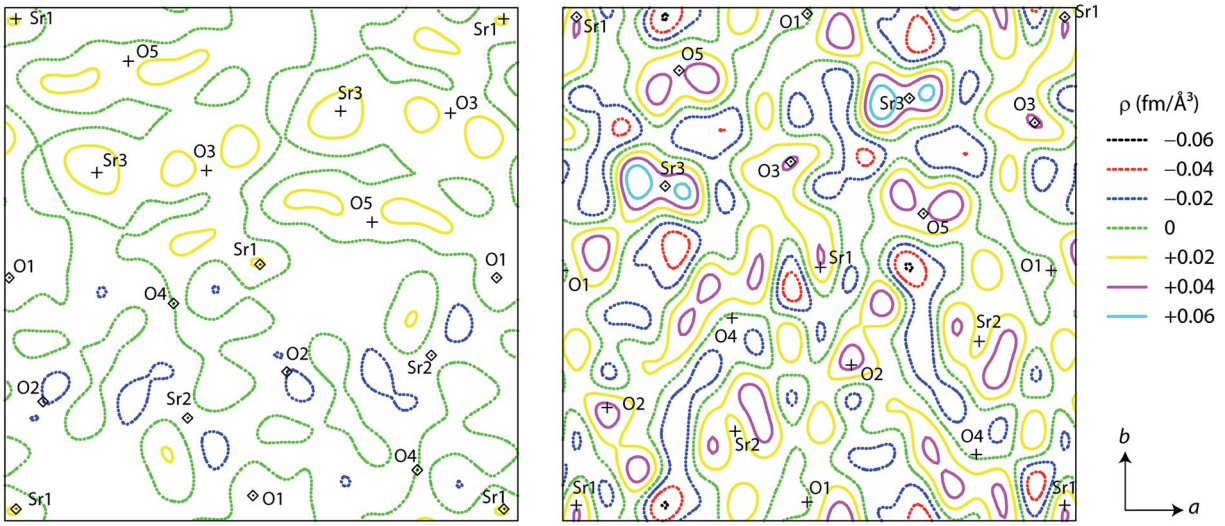

Fig. 6 Difference Fourier nuclear density for $Li_xSr_{1-0.5x}Ta_2O_6$: (a) $x = 0.08$ and (b) $x = 0.17$. Each contour diagram shows an area of 13 × 13 Å centered at (1/2, 1/2, 1/4) and perpendicular to *c*.

underbonded at the A1 site in $Li_xSr_{1-0.5x}Ta_2O_6$, with BVS values of ≈0.5. Therefore, it is presumed that the Li/Sr mixing and disorder on the A1 site could alleviate the orthorhombic distortion. In this respect, it is noteworthy that $Li_xSr_{1-0.5x}Ta_2O_6$ may have rather complex local structures. In particular, it is highly probable that Li is displaced from the ideal A1 site, and/or that the A1-centered polyhedra are distinctly relaxed depending on the cation occupancy (Sr, Li, or vacancy).

To examine whether it is legitimate to rule out the occupation of the A3 site by Li, Fourier nuclear density calculation was employed. Table 2 briefly lists the most prominent peaks from the observed (ρ_{obs}) and difference ($\rho_{diff} = \rho_{obs} - \rho_{calc}$) profiles for $Li_{0.08}Sr_{0.96}Ta_2O_6$, $Li_{0.17}Sr_{0.92}Ta_2O_6$, $Li_{0.25}Sr_{0.88}Ta_2O_6$, and β-$SrTa_2O_6$. Fig. 6 shows the two-dimensional contour diagrams of ρ_{diff}, taken for the *ab*-plane with $z = 1/4$ which corresponds to the *c*-axial height of the A1, A2, and A3 sites. In each of the above four phases, the maximum and minimum values of ρ_{diff} were significantly smaller than the respective ρ_{obs} values. This supports the reliability of the Rietveld analysis. Particularly the absence of the notable minima (negative peak) around the A3 site strongly indicates that Li resides mostly on A1 or A2 sites.[26]

Based on the Rietveld refinement, the Li^+ conduction pathways in $Li_xSr_{1-0.5x}Ta_2O_6$ can be proposed as follows. Both A1 and A2 sites are partially filled with Li and Sr, while the A1 site has the greater vacancy fraction than A2 (Fig. 5). Apparently the Li^+ hopping may occur along the *c*-axis, that is, between A2 sites through a pentagonal window or between A1 sites through a quadrangular window. But such a migration is not likely to extend to a long range due to the presence of intervening Sr. On the other hand, the A1 and A2 sites also share faces with each other in the *ab*-plane. Each A1 site is capped with six pseudo-rhombic faces, four of which are shared by A2-centered polyhedra. Meanwhile, each A2 site is immediately surrounded by two A1 sites and three A3 sites on the *ab*-plane. Therefore, a three-dimensional network of Li^+ pathway can be suggested as shown in Fig. 7a, where all the A1 and A2 sites are interconnected with one another. Here, the pseudo-rhombic faces of the A1-centered polyhedra are considered to be potential bottlenecks for the Li^+ migration.

Fig. 7b compares the window sizes, represented by the two diagonal lengths, of the rhombic faces adjoining A1 and A1 sites (along ⟨001⟩), and those adjoining A1 and A2 sites (along ⟨120⟩ or ⟨210⟩). In β-$SrTa_2O_6$ and $Li_{0.08}Sr_{0.92}Ta_2O_6$, the four faces between A1 and A2 sites were similar in size and were more distorted than those between A1 sites. However, in the phases with $x = 0.17$ and 0.25, the A1-centered polyhedra (distorted cuboctahedra) were formed with more irregular shapes. In any case, the rhombic windows, either the A1–A2 or A1–A1 types, were smaller than the pentagonal window between two A2 sites. This implies that the Li^+ hopping should be faster in the *c*-

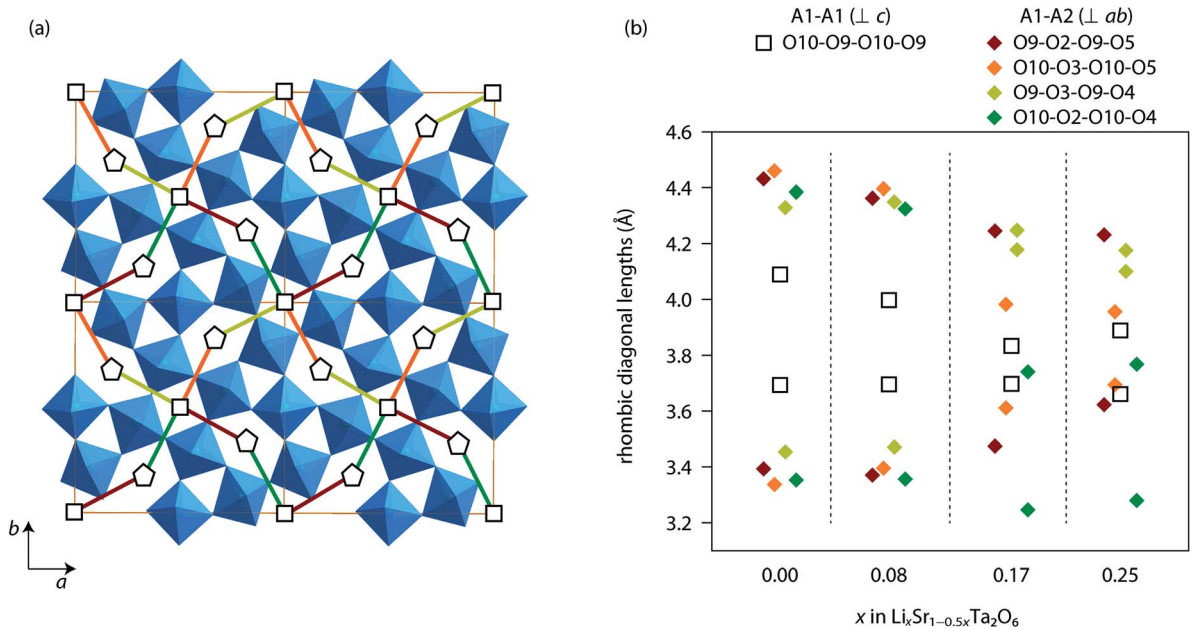

Fig. 7 (a) Two-dimensional connectivity among the A1 and A2 cavities in the TTB lattice and (b) window sizes of the A1-centered polyhedra, represented by the diagonal lengths of the rhombic faces. In (a) open pentagons and squares represent the vertical channels running along *c*-axis.

direction than in the *ab*-plane. However, it should be reminded that the long range Li^+ migration in $Li_xSr_{1-0.5x}Ta_2O_6$ will necessarily include the hopping between A1 and A2 sites. As the Li content in $Li_xSr_{1-0.5x}Ta_2O_6$ increases, the A1–A2 window gets smaller, which seems to be in part responsible for the decrease of the overall Li^+ mobility. Moreover, the increase of Li content concurrently removes the vacancy of the A1/A2 sites, for instance, from $Li_{0.08}Sr_{0.96}\square_{0.16}Ta_2O_6$ ($x = 0.08$) to $Li_{0.25}Sr_{0.88}\square_{0.07}Ta_2O_6$ ($x = 0.25$). In this regard, the observed variation of σ_{Li} in $Li_xSr_{1-0.5x}Ta_2O_6$ can be explained by taking into account the carrier concentration, site availability, and the activation of carrier migration. It is suggested that the ionic conductivity of the TTB phase would be optimized far below the full occupation of the A1 and A2 sites, and also by using a composition that can provide enlarged windows for the A1-centered cavities.

4. Conclusions

Neutron Rietveld and Fourier map analyses were employed to examine the intracrystalline structure of TTB $Li_xSr_{1-0.5x}Ta_2O_6$, from which a three-dimensional Li^+ pathway is suggested. A close examination indicated that the A1 sites, which have the distorted cuboctahedral environments, play an essential role for the long-range Li^+ migration within $Li_xSr_{1-0.5x}Ta_2O_6$. The increase of x in $Li_xSr_{1-0.5x}Ta_2O_6$ leads to the higher carrier concentration, but accompanies an adverse structural effect on the Li^+ mobility. Particularly, in the region of $x > 0.17$, the increase of Li^+ concentration is more than offset by the combined effect of two factors: the distortion of the rhombic window of the A1-centered polyhedra and the annihilation of the vacancy sites.

Conflicts of interest

There are no conflicts to declare.

Acknowledgements

This work was supported by the Yeungnam University Research Grant (2016A380034).

References

1 A. Magneli, Crystal structure of tetragonal potassium tungsten bronze, *Ark. Kemi*, 1949, **1**, 213–221.
2 A. Magneli and B. Blomberg, Contribution to the knowledge of the alkali tungsten bronzes, *Acta Chem. Scand.*, 1951, **5**, 372–378.
3 A. Magneli, Studies on the hexagonal tungsten bronzes of potassium, rubidium, and cesium, *Acta Chem. Scand.*, 1953, **7**, 315–324.
4 P. G. Dickens and M. S. Whittingham, The tungsten bronzes and related compounds, *Q. Rev., Chem. Soc.*, 1968, **22**, 30–44.
5 J. D. Guo and M. S. Whittingham, Tungsten oxides and bronzes: Synthesis, diffusion and reactivity, *Int. J. Mod. Phys. B*, 1993, **7**, 4145–4164.
6 Y. Han, M. Yang, Y. Zhang, J. Xie, D. Yin and C. Li, Tetragonal tungsten bronze framework as potential anode for Na-ion batteries, *Chem. Mater.*, 2016, **28**, 3139–3147.
7 Y. Lee, T. Lee, W. Jang and A. Soon, Unraveling the intercalation chemistry of hexagonal tungsten bronze and its optical responses, *Chem. Mater.*, 2016, **28**, 4528–4535.
8 J. Hu, Y. Zhang, D. Cao and C. Li, Dehydrating bronze iron fluoride as a high capacity conversion cathode for lithium batteries, *J. Mater. Chem. A*, 2016, **4**, 16166–16174.

9 A. Simon and J. Ravez, Solid-state chemistry and non-linear properties of tetragonal tungsten bronzes materials, *C. R. Chim.*, 2006, **9**, 1268–1276.

10 X. Zhu, M. Fu, M. C. Stennett, P. M. Vilarinho, I. Levin, C. A. Randall, J. Gardner, F. D. Morrison and I. M. Reaney, Crystal-chemical framework for relaxor *versus* normal ferroelectric behavior in tetragonal tungsten bronzes, *Chem. Mater.*, 2015, **27**, 3250–3261.

11 E. Kendrick, M. S. Islam and P. R. Slater, Investigation of proton conduction in the tetragonal tungsten bronze niobates: $A_{0.6}(M, Nb)O_3$ (A = Sr, Ba; M = Mg, Ti), *Solid State Ionics*, 2005, **176**, 2975–2978.

12 V. Hornebecq, J. M. Reau, A. Villesuzanne, C. Elissalde and J. Ravez, Ionic conductivity, ferroelectricity and chemical bonding in TKWB type ceramics of the $K_6Li_4Ta_{10}O_{30}$–$Pb_5Ta_{10}O_{30}$ system, *J. Mater. Chem.*, 1998, **8**, 2423–2428.

13 X. Kuang, F. Pan, J. Cao, C. Liang, M. R. Suchomel, F. Porcher and M. Allix, Defect structure, phase separation, and electrical properties of nonstoichiometric tetragonal tungsten bronze $Ba_{0.5-x}TaO_{3-x}$, *Inorg. Chem.*, 2013, **52**, 13244–13252.

14 A. Kuhn, H. Bashir, A. L. Dos Santos, J. L. Acosta and F. Garcia-Alvarado, New protonic solid electrolyte with tetragonal tungsten bronze structure obtained through ionic exchange, *J. Solid State Chem.*, 2004, **177**, 2366–2372.

15 V. Hornebecq, J. M. Reau and J. Ravez, New Li^+ ferroelectric conductors with tetragonal tungsten bronze structure, *Solid State Ionics*, 2000, **127**, 231–240.

16 M. L. Sanjuan, A. Kuhn, M. T. Azcondo and F. Garcia-Alvarado, Proton and deuteron exchange in TTB-like $Na_{1.2}Nb_{1.2}W_{0.8}O_6$: structural characterization and spectroscopic study, *Eur. J. Inorg. Chem.*, 2008, 49–58.

17 L. Huo, H. Zhao, F. Mauvy, S. Fourcade, C. Labrugere, M. Pouchard and J. C. Grenier, Synthesis and mixed conductivity of ammonium tungsten bronze with tunneling structures, *Solid State Sci.*, 2004, **6**, 679–688.

18 I. M. Szilagyi, J. Madarasz, G. Pokol, P. Kiraly, G. Tarkanyi, S. Saukko, J. Mizsei, A. L. Toth, A. Szabo and K. Varga-Josepovits, Stability and controlled composition of hexagonal WO_3, *Chem. Mater.*, 2008, **20**, 4116–4125.

19 H. D. Han, C. S. Park, B.-K. Min, Y. Paik, W. Jung and Y. I. Kim, Tungsten bronze Li^+ conductor $Li_xSr_{1-0.5x}Ta_2O_6$ ($0 < x \leq 0.31$) prepared by solid state ion exchange, *J. Alloys Compd.*, 2017, **726**, 913–921.

20 E. Lee, C. H. Park, D. P. Shoemaker, M. Avdeev and Y. I. Kim, Crystal structure analysis of tungsten bronzes β-$SrTa_2O_6$ and β′-$SrTa_2O_6$ by synchrotron X-ray and neutron powder diffraction, *J. Solid State Chem.*, 2012, **191**, 232–238.

21 A. C. Larson, R. B. von Dreele, *General Structure Analysis System (GSAS), Los Alamos National Laboratory Report No. LAUR 86-748*, 1994.

22 B. H. Toby, EXPGUI, a graphical user interface for GSAS, *J. Appl. Crystallogr.*, 2001, **34**, 210–213.

23 V. F. Sears, Neutron scattering lengths and cross sections, *Neutron News*, 1992, **3**, 26–37.

24 Coherent neutron scattering lengths (b in fm) are −1.90 (Li), 7.02 (Sr), 6.91 (Ta), and 5.803 (O).

25 R. D. Shannon, Revised effective ionic radii and systematic studies of interatomic distances in halides and chalcogenides, *Acta Crystallogr.*, 1976, **A32**, 751–767.

26 M. Perez-Estebanez, J. Isasi-Marin, D. M. Tobbens, A. Rivera-Calzada and C. Leon, A systematic study of Nasicon-type $Li_{1+x}M_xTi_{2-x}(PO_4)_3$ (M: Cr, Al, Fe) by neutron diffraction and impedance spectroscopy, *Solid State Ionics*, 2014, **266**, 1–8.

